QuickScan Enhanced Multi-Organ MRI Segmentation: A Deep Learning Perspective

Arvind Channarayapatna Srinivasa[1], Seema S Bhat[2], Dikendra Baduwal[3], Sim Zheng Ting Jordan[4] Shamshekar S Patil[5], Ashwin Amarapur[2], KN Bhanu Prakash[1]

[1] Bioinformatics Institute (BII), Agency of Science, Technology and Research (A*STAR), 30 Biopolis Street, #07-01 Matrix, Singapore 138671, Republic of Singapore
[2] Aikenist Technologies Pvt. Ltd, Bengaluru, India
[3] Vel Tech Rangarajan Dr. Sagunthala R&D institute of science and technology, Chennai, India
[4] Department of Diagnostic Radiology, Tan Tock Seng Hospital, 11 Jln Tan Tock Seng, Singapore 308433
[5] Dr Ambedkar Institute of Technology, Bengaluru, India

Corresponding Author

Arvind CS
Bioinformatics Institute (BII),
Agency of Science, Technology and Research (A*STAR),
30 Biopolis Street, #07-01 Matrix, Singapore 138671, Republic of Singapore
arvindcs@bii.a-star.edu.sg

Abstract:

High-resolution Magnetic Resonance Imaging (MRI) is essential for clinical diagnostics but requires long scan times, leading to patient discomfort and motion artifacts. Quick-acquisition techniques shorten scan times but often compromise image quality due to increased noise and reduced contrast, hindering accurate segmentation crucial for diagnosis and treatment planning. To address this issue, we utilized a GAN-based QuickScan, MR scan enhancement algorithm that improves MRI contrast quality and segmentation accuracy without extending scan times.

Method: An end-to-end framework was developed with (i) anonymiser and BIDS based data organizer, (ii) GAN-based image enhancement as pre-processing, (iii) Deep-learning models-based Assembly Net for brain scans and Attention based Residual U-Net for abdomen and thigh quantitative segmentation. Statistical and quantitative metrics were computed to evaluate the image enhancement and segmentation. 30 brain scans (5,400 slices) and 32 abdomen & Thigh scans (1,920 slices) each acquired from different MRI scanners (GE, Siemens, Toshiba) with varying protocols were used in the study.

Results: Significant improvements in image quality metrics were observed, with SNR and CNR increasing for brain scans from 28.44 to 42.92 ($p<0.001$) and 11.88 to 18.03 ($p<0.001$), respectively. Abdominal scans showed SNR rising from 35.30 to 50.24 ($p<0.001$) and CNR from 10,290.93 to 93,767.22 ($p<0.001$). A double-blinded evaluation highlighted enhanced visibility of intricate anatomical structures, muscle boundaries, tissue interfaces, and improved bias field correction. Segmentation improvements included: Abdominal regions: SSAT (+1%, 0.97 to 0.98), DSAT (+2%, 0.93 to 0.95), VAT (+12%, 0.88 to 0.985), and Thigh regions: muscle (+21%, 0.72 to 0.87), IMAT (+9%, 0.79 to 0.86). Brain segmentation showed no significant differences.

Conclusion:.
The GAN-based QuickScan framework significantly enhances MR image quality and segmentation accuracy without increasing scan times, demonstrating its potential to address the limitations of rapid MRI acquisition. Improved SNR, CNR, and segmentation metrics highlight its effectiveness for abdominal and thigh scans, enabling more precise diagnostics and treatment planning, while maintaining efficiency and patient comfort.

Introduction

Magnetic Resonance Imaging (MRI) is a critical diagnostic tool in modern medicine, providing detailed images of various anatomical regions. However, traditional MRI techniques can be time-consuming and susceptible to motion artifacts, particularly in patients who are unable to remain still, such as children or those with claustrophobia. Accelerated MRI acquisitions address these challenges but can affect the quality of the scans.

Fast MR imaging is an advanced MRI technique designed to significantly reduce scan times while maintaining high-quality images [1, 2]. This method utilizes faster gradient systems and efficient pulse sequences to accelerate image acquisition, ideal for restless, claustrophobic patients and emergencies. It includes techniques like echo planar imaging (EPI), fast spin-echo (FSE), and gradient echo sequences [3], each tailored for specific diagnostic needs. The primary benefits are reduced scan times, decreased motion artifacts [4], and improved patient compliance, though there can be trade-offs in resolution or contrast. Continuous technological advancements in this field aim to further minimize scan duration while enhancing image quality and patient safety, underscoring its growing significance in diverse clinical settings.

Maria Elena Riccioni et al. [5] compared the accuracy of fast magnetic resonance imaging (MRI) using HASTE sequences with helical computed tomography (CT) in diagnosing bowel obstruction, finding that fast MRI with HASTE sequences improved detection accuracy by 25% compared to helical CT. Despite their advantages, magnetic resonance (MR) scans face image quality issues that can impact diagnosis and treatment plans, leading researchers to develop machine and deep learning methodologies in recent years to enhance quick MR scan quality.

Zhaolin Chen et al. [6] developed a deep neural network (DNN) model which converts motion-corrupted images into motion-free ones. Guangming Zhu et al. [7] proposed a Recurrent Neural Network (RNN) that detects motion artifacts with 95% accuracy and improves signal-to-noise and contrast-to-noise ratios, resulting in enhanced image quality. Javier Villanueva-Meyer et al. [8] stated that AI-based software can maintain high-quality standards for 3D brain MRI sequences while reducing scan times by 45%, significantly enhancing the patient experience and scanner efficiency without compromising diagnostic quality.

A study by Almansour et al. [9] demonstrated the benefits of combined deep learning-based super-resolution and partial Fourier reconstruction in abdominal MRI at 3 Tesla. This approach shortened breath-hold time, improved image sharpness, and enhanced lesion conspicuity. Similarly, Chu et al. [10] found that deep learning image reconstruction (DLIR) at a high level significantly improved image quality and diagnostic confidence compared to adaptive statistical iterative reconstruction in abdominal dual-energy computed tomography.

Zhang et al. [11] utilized deep learning-based convolutional recurrent neural networks to enhance the reconstruction process of under-sampled non-Cartesian dynamic abdominal MRI data. This method improved image quality and reduced computational time. Kim et al. [12] focused on deep learning-based k-space-to-image reconstruction and super-resolution for diffusion-weighted imaging in whole-spine MRI, further advancing imaging capabilities.

Racine et al. [13] found that deep learning reconstruction outperformed traditional methods like filtered back-projection and model-based iterative reconstruction in detecting abdominal lesions across various dose levels. Similarly, Bornet et al. [14] emphasized the clinical acceptance of deep learning reconstruction for abdominal CT imaging, focusing on objective and subjective image quality and low-contrast detectability assessment.

Study Objectives

The primary aim of this study is to evaluate the effect of image enhancement techniques in the QuickScan application on the performance of deep learning-based segmentation and quantification models in various anatomical regions. Our investigation is focused on two key aspects:

1. **Quantitative Evaluation of QuickScan Application-Based Image Enhancement:**
    - **Image Enhancement:** To rigorously evaluate the efficacy of the QuickScan application in enhancing medical images, particularly its ability to improve visibility and clarity of anatomical structures, which are often challenging to discern due to factors like noise, low resolution, or contrast.
    - **Suitability for Quantitative Segmentation:** To assess the effectiveness of QuickScan-enhanced images for subsequent use in quantitative segmentation tasks. This includes evaluating the accuracy, precision, and robustness of segmentation when applied to various organ systems.
2. **Examination of the Impact on Deep Learning Model Performance:**
    - **Segmentation and Quantification Accuracy:** To analyze the effect of image enhancement by QuickScan on the performance of deep learning models in the segmentation and quantification of anatomical regions. This study will explore whether enhanced images improve model outcomes by providing higher-quality input data.
    - **Anatomical Regions of Focus:**
        - **Brain:** Investigate the impact on brain tissue segmentation and volumetric quantification, with particular attention to fine structures such as cortical layers and subcortical regions.
        - **Abdomen and Thigh Regions:** Assess the effects of enhancement on abdominal and thigh imaging, where organ boundaries and structures such as adipose tissue, muscles, and organs like the liver, kidneys, and femur are key targets for segmentation.

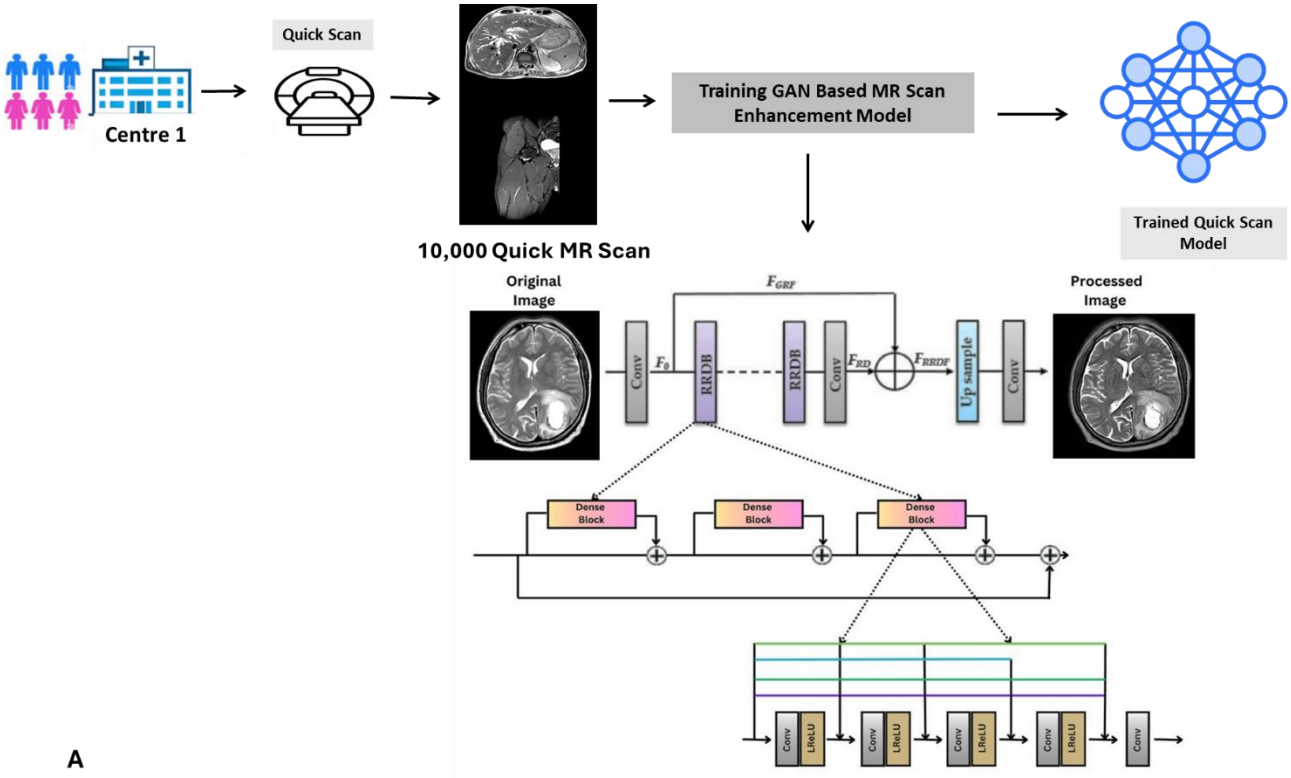
Through a combination of image processing metrics and deep learning-based segmentation models, this study aims to provide a comprehensive evaluation of how QuickScan's image enhancement capabilities contribute to improving medical image analysis tasks. Specifically, we hypothesize that the enhancements offered by QuickScan will lead to a measurable improvement

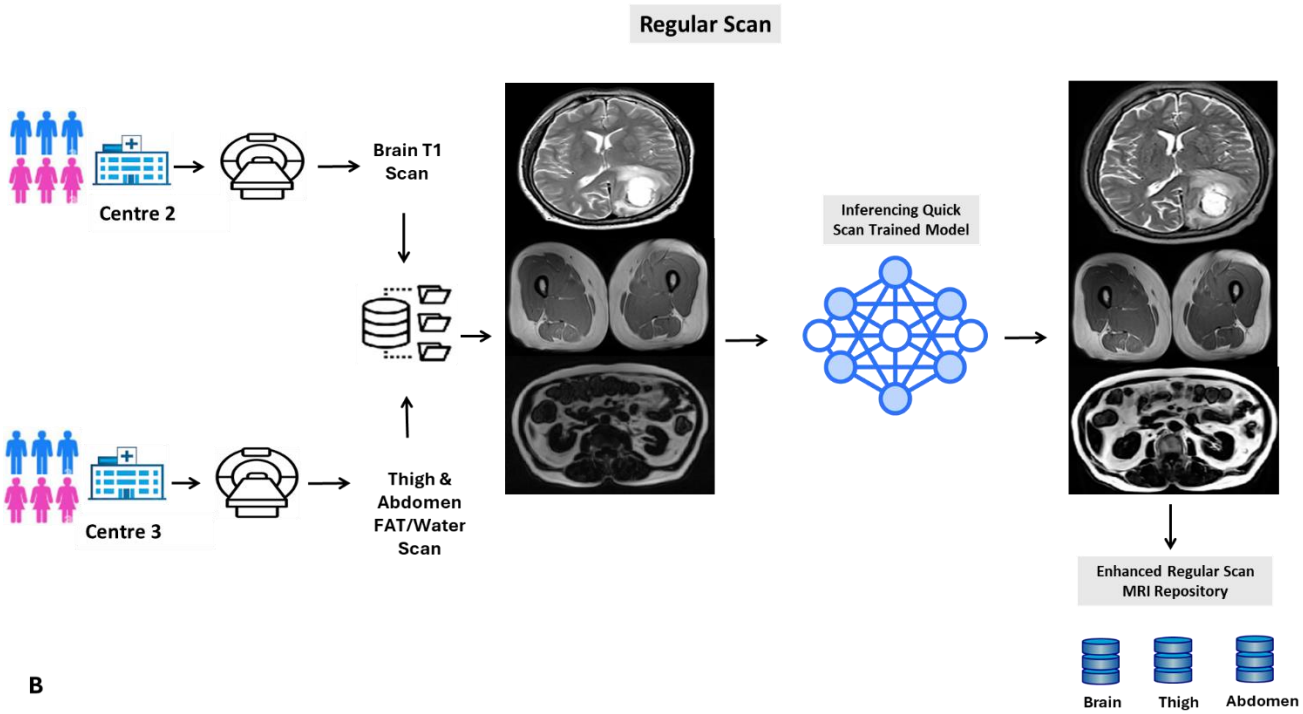
in the performance of segmentation models across the brain, abdomen, and thigh regions, offering insights into its potential applications in clinical workflows for diagnostics and treatment planning.

To achieve this, we developed a comprehensive, integrated framework (Figure-1) encompassing the following modules:

- Anonymization of scans and BIDS-based DICOM to NIfTI conversion and organization
- Image enhancement through the GAN-based QuickScan application
- Deep learning-based segmentation for Brain, Abdomen, and Thigh regions
- Statistical and volumetric analysis

MR scans in DICOM format were anonymized, converted, and organized into BIDS format-based repositories to streamline storage and management of large datasets. Image enhancement was performed using the QuickScan application (developed by Aikenist) prior to training with deep learning models, as outlined in Figure 1. For quantitative volumetry of brain images, the Assembly Net model was employed, while an Attention-based ResUNet (Attention ResUNet) model was used for segmentation of the thigh and abdomen regions.





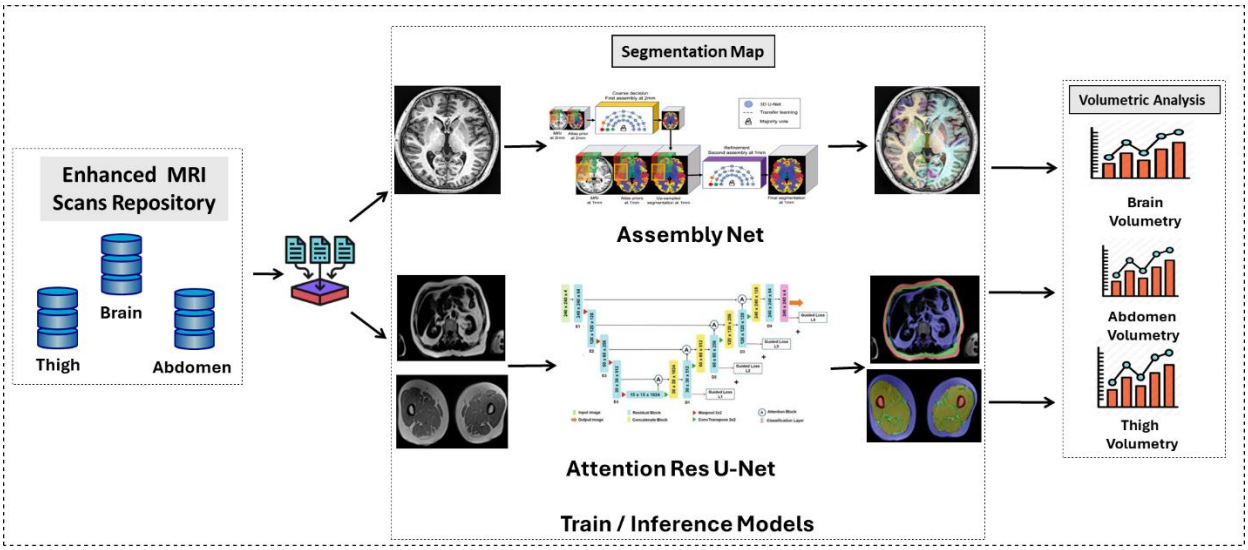


Figure (1): Workflow of the Proposed MRI Scan Enhancement and Segmentation Framework

This figure illustrates the end-to-end processing pipeline for MRI scan enhancement and segmentation. The workflow includes: (1) Data Acquisition – MRI scans collected from Centre 1: JSS Medical College, Mysore, India; Centre 2: Sengkang General Hospital (SKH), Singapore; and Centre 3: Tan Tock Seng Hospital (TTSH), Singapore. (2) QuickScan-based Enhancement – A GAN-based MRI enhancement model is trained using 10,000 Quick MR scans, improving image quality and contrast. (3) Segmentation and Quantitative Analysis – Enhanced scans are further

processed for brain, abdomen, and thigh segmentation using AssemblyNet and AttentionRes U-Net models to facilitate detailed quantitative analysis.

Methodology

Imaging Sequences and Methodology Overview

Image Acquisition

Centre 1: Table 1 provides a comprehensive summary of the imaging sequences used in this study at Centre 1. A total of 10,000 MRI scans were acquired, encompassing T1-weighted, T2-weighted, Proton Density (PD) with fat suppression, Fluid Attenuated Inversion Recovery (FLAIR), and Short Tau Inversion Recovery (STIR) sequences across multiple scanner platforms, including Philips, Siemens, GE, and Canon. These sequences were selected for their ability to capture a wide range of tissue contrasts, which are essential for evaluating both structural and functional characteristics of various anatomical regions.

The study included a diverse participant cohort aged 20 to 80 years, comprising both male and female subjects to ensure broad generalizability across age groups and sexes. The targeted anatomical regions included the brain, spine, musculoskeletal system, abdomen, pelvis, and thigh, providing a comprehensive dataset to assess the efficacy of QuickScan-based image enhancement and its impact on deep learning segmentation models.

Centre 2

Centre 2: A total of 1,287 cognitively unimpaired Singaporean individuals (576 males, 711 females) aged 1 to 100 years were analyzed using 3D T1-weighted MRI scans collected at Sengkang General Hospital (SKH). The MRI scans were acquired using a 3D T1-weighted MPRAGE sequence with a voxel resolution of 1 mm^3, ensuring high-quality anatomical detail.

To maintain consistency across subjects, all scans were performed using a single MRI scanner at SKH and were aligned to the anterior and posterior commissures (AC-PC line) to ensure uniform anatomical positioning. Quality control was conducted by three board-certified radiologists, who independently reviewed each MRI scan and excluded any that did not meet the established criteria for data integrity and imaging quality.

Centre 3: The Geri-LABS study is a prospective cohort study examining biomarkers related to early signs of sarcopenia and its potential connection to frailty and functional decline in older Asian adults above. A total of 190 abdominal MRIs were taken from participants using a 3T Siemens Magnetom Trio MRI scanner. Ethics approval for the study was obtained by the Domain Specific Review Board of the National Healthcare Group and informed written consent was obtained from the participant. The mean participant age was 67.85 years, with a mean BMI of 23.75 kg/m^2. Participants were predominantly female (69.5%) and of Chinese descent (91.6%). Notable

comorbidities include hypertension (46.8%), hyperlipidaemia (65.8%), and Type II diabetes mellitus (21.1%).

The MRI scans were specifically 3D-modified Dixon T1-weighted images with dual-echo VIBE and T2* correction. MRI scans captured 40–60 slices in the pelvic area and 20–30 slices in the thigh area for each patient. These slices had a thickness of 5 mm and an in-plane resolution of 1.56 × 1.56 mm, without any slice gaps. For the T1-weighted scans, the settings used were a TR of 6.62 ms, a TE of 1.225 ms, an FA of 10°, and an acquisition bandwidth of 849 Hz/pixel. The system produced water- and fat-only images from the combination of in-phase and out-phase images. Any fat-water discrepancies in the images were corrected during the image reconstruction phase in the scanner.

All the centre study was conducted with approval from the Domain Specific Review Board (DSRB) and the Institutional Review Board (IRB), ensuring compliance with ethical standards and the protection of participant rights and privacy. To safeguard patient confidentiality, all MRI DICOM scans were anonymized before processing.

Study Design

The study is divided into two distinct phases:

1. **Phase 1: Evaluation of QuickScan for Time Efficiency and Visual Quality**
    - **Objective:** To assess the time-saving potential and visual enhancement of QuickScan application in comparison to standard imaging protocols.
    - **Metrics Assessed:**
        - **Time Efficiency:** Quantification of scan acquisition time differences between QuickScan and standard protocols.
        - **Signal-to-Noise Ratio (SNR):** An evaluation of the overall signal clarity in the enhanced images, ensuring that noise reduction does not compromise important anatomical details.
        - **Contrast-to-Noise Ratio (CNR):** Assessment of tissue contrast relative to background noise, ensuring better delineation of anatomical boundaries and pathological regions.
        - **Radiologist Evaluations:** Expert radiologists will subjectively evaluate image quality based on diagnostic utility, visibility of critical structures, and overall interpretability.

This phase will establish the feasibility of QuickScan for improving image acquisition speed and overall visual quality, making it a potential candidate for routine clinical practice.

2. **Phase 2: Segmentation and Quantification with QuickScan-Enhanced Images**

    - **Objective:** To investigate the performance of deep learning-based segmentation models on QuickScan-enhanced images, specifically focusing on anatomical accuracy and quantification precision.

    - **Metrics Assessed:**

        - **Dice Similarity Coefficient (DSC):** The Dice index will be used as the primary metric to evaluate segmentation accuracy. This metric quantifies the overlap between model predictions and ground truth, providing a clear indication of the effectiveness of segmentation on enhanced images.

        - **Segmentation of Anatomical Regions:** Deep learning models will be trained and validated for various anatomical regions, including brain parenchyma, spinal cord, abdominal organs, and musculoskeletal structures. The effect of QuickScan enhancement on model performance across these regions will be assessed, providing insights into the versatility of the enhancement for different tissue types and anatomical structures.

Table 1: Outline of study details

Category	Details
Sequences	T_1, T_2, PD (Fat sup), FLAIR, STIR
Scanners	Philips, Siemens, GE, Canon
Anatomy	Brain, Spine, MSK, Abdomen, Pelvis, Thigh
Age	20 yrs. ~ 80 yrs. (M/F)
Study	**1) Quick scan + App → Time efficiency / Visual**
	2) Regular scan + App → Segmentation / Quantification
Metrics	**Study -1: Time improvement, SNR, CNR, Radiologists evaluation**
	Study -2: Dice statistical index

Pre-Processing

The preprocessing pipeline involves two main steps: (1) data organization using the Brain Imaging Data Structure (BIDS) standard and (2) image contrast/resolution enhancement with QuickScan application.

(i) BIDS-Conversion

The BIDS format standardizes data organization, using the BIDS library to convert DICOM images for abdomen, thigh, and brain datasets into NIfTI file format (.nii.gz) and systematically arranging them in their respective directories within a designated repository.

(ii) QuickScan based image contrast enhancement

The QuickScan enhancement model is a state-of-the-art deep learning framework designed to improve the quality of both rapid-acquisition and standard MRI scans by addressing common challenges such as noise, blurring, and resolution loss. The architecture is structured into several key components, as illustrated in the diagram.

The process begins with a low-resolution input image (256 x 256), which is passed through an initial convolutional layer to extract basic features (F_0) [15]. These features are then fed into a sequence of Residual-in-Residual Dense Blocks (RRDBs), which serve as the core of the architecture [16]. Each RRDB, shown in the middle section of the diagram, is composed of multiple Dense Blocks that stack convolutional layers with activation functions like Leaky ReLU [17]. The dense connections within each block ensure efficient feature reuse, while residual connections improve training stability and gradient flow. This hierarchical feature extraction allows the model to learn both low-level and high-level image details [16, 17].

After passing through the RRDBs, the extracted features are further refined using an additional convolutional layer to produce an enhanced feature map (F_1) [15]. This map is subsequently processed by the upsampling module, depicted in the diagram as a light blue block. The upsampling module increases the spatial resolution, effectively transforming the low-resolution input into a high-resolution feature map (F_2) [18]. The final convolutional layer then reconstructs the enhanced, super-resolved image, producing an output of size 512 x 512 [15].

The diagram also highlights the Dense Blocks within the RRDBs in greater detail. Each Dense Block consists of several convolutional layers connected by dense skip connections, ensuring that each layer receives inputs from all previous layers. This structure enhances feature propagation and improves the model's ability to learn complex patterns [16, 17].

The integration of attention mechanisms (temporal and spatial) within the deblurring module allows the model to focus on regions prone to motion and blurring artifacts [19]. Additionally, the GAN-based super-resolution component further enhances the model's ability to reconstruct high-frequency details, which is critical for revealing subtle pathological changes and intricate anatomical features [20]. The model employs a custom loss function combining pixel-wise loss for reconstruction accuracy and perceptual loss to enhance visual fidelity, as indicated by the quality of the output image in the diagram [21].

The QuickScan deep learning model was fine-tuned on a system with an Intel Core i5 processor, 31.2 GiB RAM, NVIDIA RTX 2080 GPU, Ubuntu 20.04.6 LTS, and 11.3 TB storage. Developed using PyTorch, the model was trained on a dataset of over 10,000 MRI images from diverse

anatomical regions, scanners, and vendors. Clinical evaluation of 500 cases demonstrated significant improvements in diagnostic confidence and accuracy, with QuickScan-enhanced images achieving quality comparable to or exceeding high-resolution scans. The model's advanced architecture, detailed in the diagram (Figure-2), establishes a benchmark for MRI imaging, improving diagnostic precision and patient outcomes.

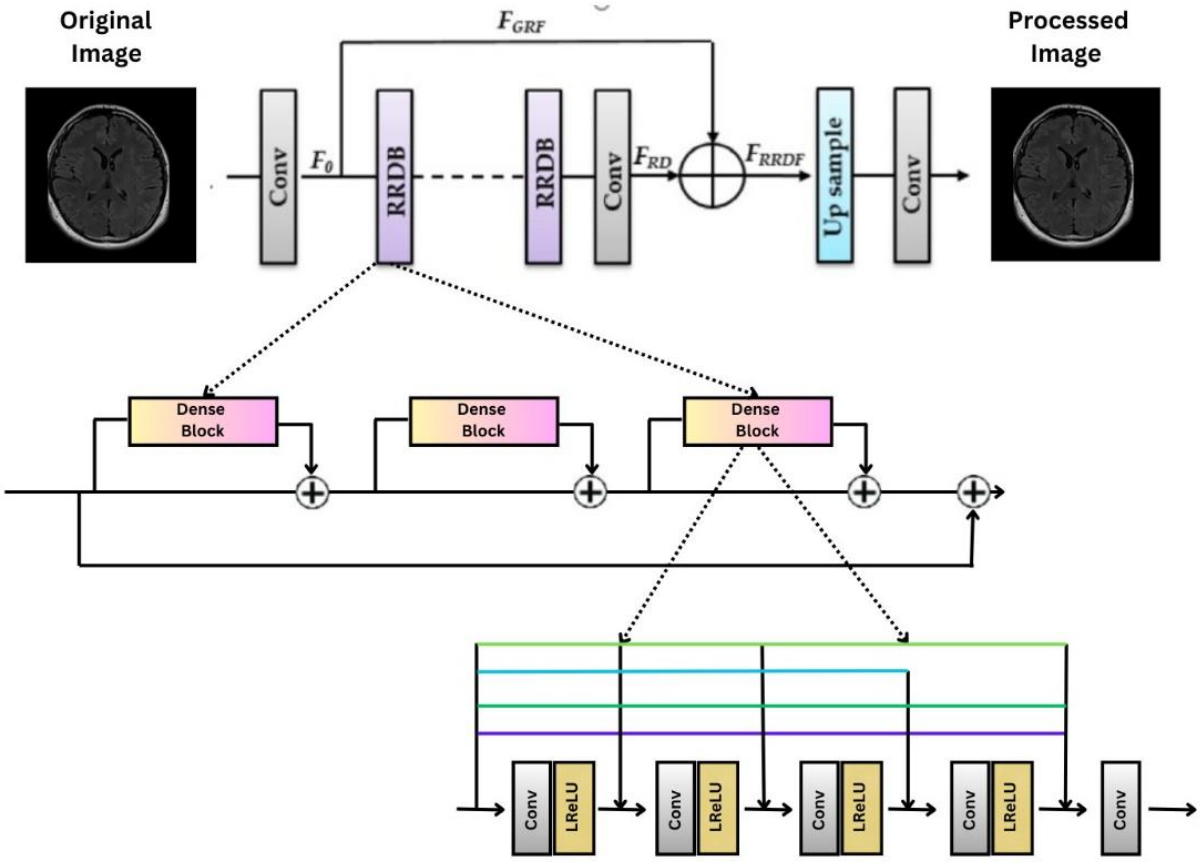


Figure 2a: QuickScan Model Architecture

The diagram depicts the QuickScan model's architecture, highlighting the initial convolutional layer, Residual-in-Residual Dense Blocks (RRDBs), and the GAN-based super-resolution module. The model processes a low-resolution MRI input to produce a high-resolution output .

Segmentation

3D Whole Brain MRI Segmentation: Assembly Net

The 3D whole brain MRI segmentation in this study utilizes AssemblyNet, a robust segmentation framework built on the U-Net architecture, which can handle limited data and efficiently perform rapid segmentation for biomedical images [22]. AssemblyNet leverages a unique ensemble approach, consisting of 250 U-Nets arranged as two "assemblies," with each assembly including 125 3D U-Nets aligned along the three-dimensional axes. Each U-Net processes overlapping regions of the brain, enabling knowledge transfer between neighboring networks and improving segmentation accuracy. The final segmentation output is obtained using a majority vote, combining results from overlapping areas to ensure consistent and accurate segmentation.

Atlas priors are generated through nonlinear registration at 2 mm^3 and 1 mm^3 resolutions, which provide spatial reference for segmentation refinement. Coarse segmentation begins at a resolution of 2 x 2 x 2 mm^3 and is subsequently upsampled to 1 x 1 x 1 mm^3 for fine segmentation, integrating atlas priors and raw images into the process. For quality assurance, AssemblyNet incorporates a deep learning-based quality control module called RegQCNet, which assesses registration accuracy by calculating residual misalignment between images before and after registration. This ensures reliable segmentation outputs [23].

The implementation of AssemblyNet in this study is based on its publicly available framework for segmenting brain regions, which can be accessed through its GitHub repository [24].

ARU-Net: Attention Residual U-Net for Abdomen and Thigh Region Segmentation

This study introduces an enhanced version of the U-Net architecture, termed Attention Residual U-Net (ARU-Net), specifically designed for the segmentation of abdomen and thigh regions from MR scans. The input to the network consists of Dixon fat-only MR sequences, which provide detailed visualization of fat distribution and anatomical structures in the abdomen and thigh regions. ARU-Net builds upon the U-Net framework [25], incorporating residual connections [26] and attention gates (AGs) [27] to improve segmentation performance. The encoder-decoder structure of U-Net efficiently extracts and refines hierarchical image features, while residual connections address the vanishing gradient problem, ensuring smooth gradient flow and better network convergence.

A key enhancement in ARU-Net is the integration of attention gates (AGs) [27] within skip connections. These AGs act as dynamic filters, selectively emphasizing relevant features from the encoder outputs while suppressing irrelevant or noisy background information. This mechanism improves feature propagation, leading to higher segmentation accuracy, particularly for complex anatomical structures. Furthermore, to address the challenge of class imbalance in thigh and abdomen segmentation, ARU-Net employs the focal loss function [28], defined as:

$$FL(pt) = -\alpha t \cdot (1-pt)\gamma \cdot \log(pt) \quad (1)$$

where $\alpha t=0.7$ balances class importance, and γ adjusts the focusing parameter to prioritize harder-to-classify regions.

The ARU-Net architecture comprises four encoder blocks (E1–E4) and four decoder blocks (D1–D4), each with the following components:

1. **Encoder Blocks (E1–E4):** Each encoder block includes residual connections to improve feature learning and gradient flow. Spatial resolution is reduced using 2×2 max-pooling layers to capture multi-scale contextual information [25].
2. **Decoder Blocks (D1–D4):** The decoder blocks use 2×2 transposed convolutions for up-sampling and spatial resolution recovery. Skip connections between encoder and decoder levels allow the network to combine low-level spatial details with high-level features [25].
3. **Attention Gates (AGs):** Integrated into the skip connections, AGs selectively focus on relevant encoder features while suppressing background noise, improving segmentation precision [27].
4. **Guided Losses (L1–L4):** Intermediate guided losses are applied at each decoder level to refine segmentation outputs at multiple resolutions, enhancing both convergence and performance [28].
5. **Classification Layer:** The final classification layer produces pixel-wise segmentation, distinguishing various anatomical sub-regions [25].

The input consists of Dixon fat-only MR scans from the abdomen and thigh regions. The outputs represent segmented regions, with distinct anatomical structures assigned to different classes:

Abdomen Region: Class 1: Subcutaneous fat. Class 2: Deep subcutaneous fat. Class 3: Visceral fat. **Thigh Region:** Class 1: Bone. Class 2: Intramuscular fat. Class 3: Subcutaneous fat. Class 4: Muscle.

In summary, ARU-Net introduces residual connections, attention gates, and guided losses into the U-Net framework to achieve superior segmentation performance for the abdomen and thigh regions. The attention mechanism ensures accurate segmentation by focusing on the most relevant features, while the focal loss function effectively mitigates class imbalance. These improvements make ARU-Net a powerful tool for segmentation of Dixon fat-only MR images in clinical and research setting

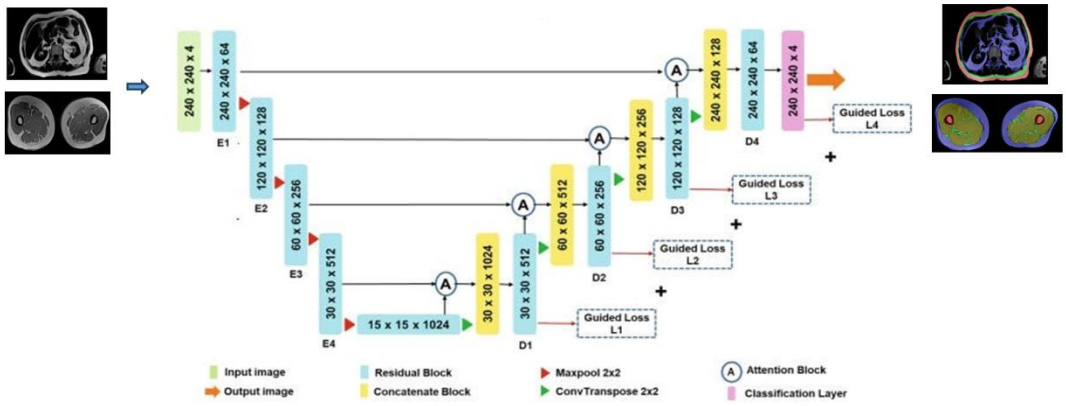


Figure 2b: Attention-Guided U-Net for Thigh and Abdomen Region Segmentation **Abdomen Region**: **Class 1**: Subcutaneous fat. **Class 2**: Deep subcutaneous fat. **Class 3**: Visceral fat. **Thigh Region**: **Class 1**: Bone. **Class 2**: Intramuscular fat. **Class 3**: Subcutaneous fat. **Class 4**: Muscle.

Training Parameters

Single contrast fat-only images of the abdomen and thigh regions from subjects with low, medium, and high-fat content were used for training. The training environment consisted of Ubuntu 22.04 OS with 128 GB of RAM and a 24 GB NVIDIA graphics processing unit. The code, written using the PyTorch framework, employed the hyperparameters of the Attention Residual U-Net model, as detailed in Table 2.

The hyperparameters used to train the Attention Residual U-Net (ARU-Net) model for abdomen and thigh segmentation are summarized in Table 2. These parameters were carefully chosen to address the unique challenges associated with segmenting Dixon fat-only MR images from subjects with varying fat content. Key hyperparameters include the use of Focal Dice Loss to mitigate class imbalance and early stopping to prevent overfitting. The difference in the number of epochs (50 for abdomen and 60 for thigh) reflects the nature of the data; on average, each abdominal scan contains around 60 slices, providing a richer dataset per subject, while thigh scans typically consist of 30–40 slices, requiring additional training iterations to achieve comparable model performance.

TABLE 2 : Hyperparameters to training AttentionResUNet for abdomen & Thigh anatomy

Parameter	Abdomen	Thigh
No. of subjects	32	55
Number of filters at each level of U-Net	16, 32, 64, 128, 256	16, 32, 64, 128, 256
Epochs	50	60
Optimizer	ADAM	ADAM
Learning rate	0.00001	0.001
Loss function	Focal dice loss	Focal dice loss

Parameter	Abdomen	Thigh
Weighted decay	2e-6	2e-6
Dropout	0.05	0.05
Patience	15	15

Evaluation Metric

To assess the performance of denoising and segmentation methods, we employed visualization techniques and quantitative evaluation metrics. Denoising performance was measured using established metrics like structural similarity index (SSIM), signal-to-noise ratio (SNR), and contrast-to-noise ratio (CNR). Segmentation accuracy was evaluated using the Dice coefficient.

Denoising Evaluation Metric

Structural Similarity Index (SSIM):

SSIM measures the similarity between images involving three factors: brightness, contrast, and structural information. It assumes that brightness and contrast changes don't affect the underlying structure of the image. The mathematical definition of SSIM is:

$$SSIM = \frac{(2\mu_m\mu_n+(k_1l)^2)(2\sigma_{mn}+(k_2l)^2)}{(\mu^2{}_m+\mu^2{}_n+(k_1l)^2)(\sigma^2{}_m+\sigma^2{}_n+(k_2l)^2)} \quad (2)$$

Here, m is the reference image, n is the denoised image, l represents the dynamic range of the grey value, μ represents the mean, and σ² represents the variance. k1 and k2 are small constants to avoid division by zero. The SSIM value ranges from 0 to 1, with a higher value indicating greater similarity between the images [29].

Mean Squared Error (MSE):

Objectively reflects the difference between corresponding pixels in two images. It's calculated as:

$$MSE = \frac{1}{xy}\sum_{i=0}^{x-1}\sum_{j=0}^{y-1}[m(i,j)-n\,(i,j)]^2 \quad (3)$$

Here, x and y represent the image width and height, respectively. m(i, j) and n(i, j) represent the grey values at coordinates (i, j) in images m and n, respectively [29].

Signal-to-Noise Ratio (SNR):

NR measures the ratio between the actual information (signal) SSS in an image and the background noise (NNN). A higher SNR indicates a better-denoised image. The SNR formula is defined as

$$SNR = 20 * log_{10}\left[\frac{S_\mu}{N_\sigma}\right] \quad (4)$$

Here, Sμ is the mean signal, and Nσ is the standard deviation of the noise. This equation is adapted from Dietrich et al. (2007) [30].

Contrast-to-Noise Ratio (CNR):

CNR measures the difference between the signal of interest and the background noise level. A higher CNR indicates better contrast between the object and its background in the denoised image. Specific definitions of CNR can vary depending on the application.

$$CNR = \left[\frac{S_\mu}{N_\mu}\right] \qquad (5)$$

Segmentation Metrics

The performance of both the AttentionRes U-Net and AssemblyNet models was evaluated using the Dice Similarity Coefficient (DSC). This metric assesses the similarity between predicted segmentation masks and ground truth segmentation labels for various anatomical sub-regions. The formula for DSC is.

$$DISC = \frac{2 * TP}{FN+TP+TN+FP} \qquad (6)$$

where TP, FN, TN, and FP represent true positives, false negatives, true negatives, and false positives, respectively. A detailed performance evaluation for each sub-region using DSC is illustrated in Figures 5 and 6, showing segmentation results for different anatomical regions. Where Abdomen: Red-SSAT, Green-DSAT, Blue-VAT, Thigh: Red-Bone, Green-IMAT, Blue-SAT, Yellow-Muscle

Results

Impact of QuickScan Application on MRI Sequence Efficiency

Table 3 and Figure 3 demonstrate the effectiveness of the QuickScan application in significantly reducing MRI scan times across various sequences and anatomical regions. The results indicate marked improvements, especially within the T_1- and T_2-weighted sequences for the brain, spine, and musculoskeletal (MSK) regions. Specifically, scan times were reduced by an average of 0.91 to 1.76 minutes, achieving statistical significance with $p \leq 0.0001$ \. These reductions highlight QuickScan's potential to enhance imaging efficiency while maintaining diagnostic quality.

Additionally, sequences such as Fluid-Attenuated Inversion Recovery (FLAIR) and Short Tau Inversion Recovery (STIR), commonly used in brain and spine imaging, also showed substantial time savings. Specialized sequences like Proton Density Fat Suppression (PDFS), which are utilized in MSK imaging, demonstrated similar improvements with notable decreases in acquisition time.

Table 3: Improvement in acquisition time using QuickScan for different anatomical regions and sequences.

Seq	Organ	No Scans	Mean regular	Mean QuickScan time (min)	Mean time difference (min)	t-value	p-value

			scan time (min)				
T_1	Brain	32	3.42	2.21	1.21	10.23	≤0.0001
	Spine	50	3.33	1.57	1.76	16.06	≤0.0001
	MSK	13	3.02	1.67	1.35	8.53	≤0.0001
T_2	Brain	249	2.07	0.44	1.63	55.42	≤0.0001
	Spine	80	3.30	1.73	1.57	21.81	≤0.0001
	MSK	5	3.30	2.39	0.91	6.42	≤0.0001
	Abdomen	7	3.69	1.68	2.01	5.52	≤0.0001
	Pelvis	3	2.94	1.39	1.55	2.12	0.101
FLAIR	Brain	22	3.27	1.60	1.67	14.79	≤0.0001
STIR	Spine	38	3.53	2.29	1.24	13.94	≤0.0001
PDFS	MSK	7	2.49	0.96	1.53	8.59	≤0.0001

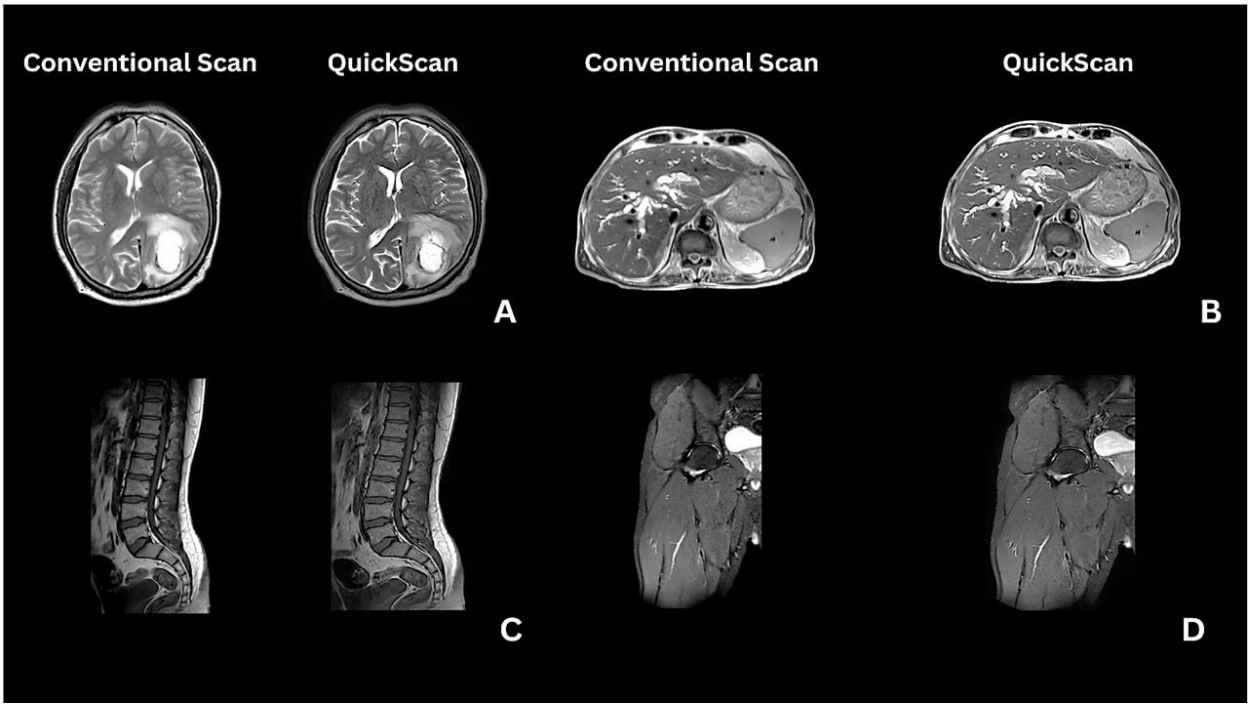
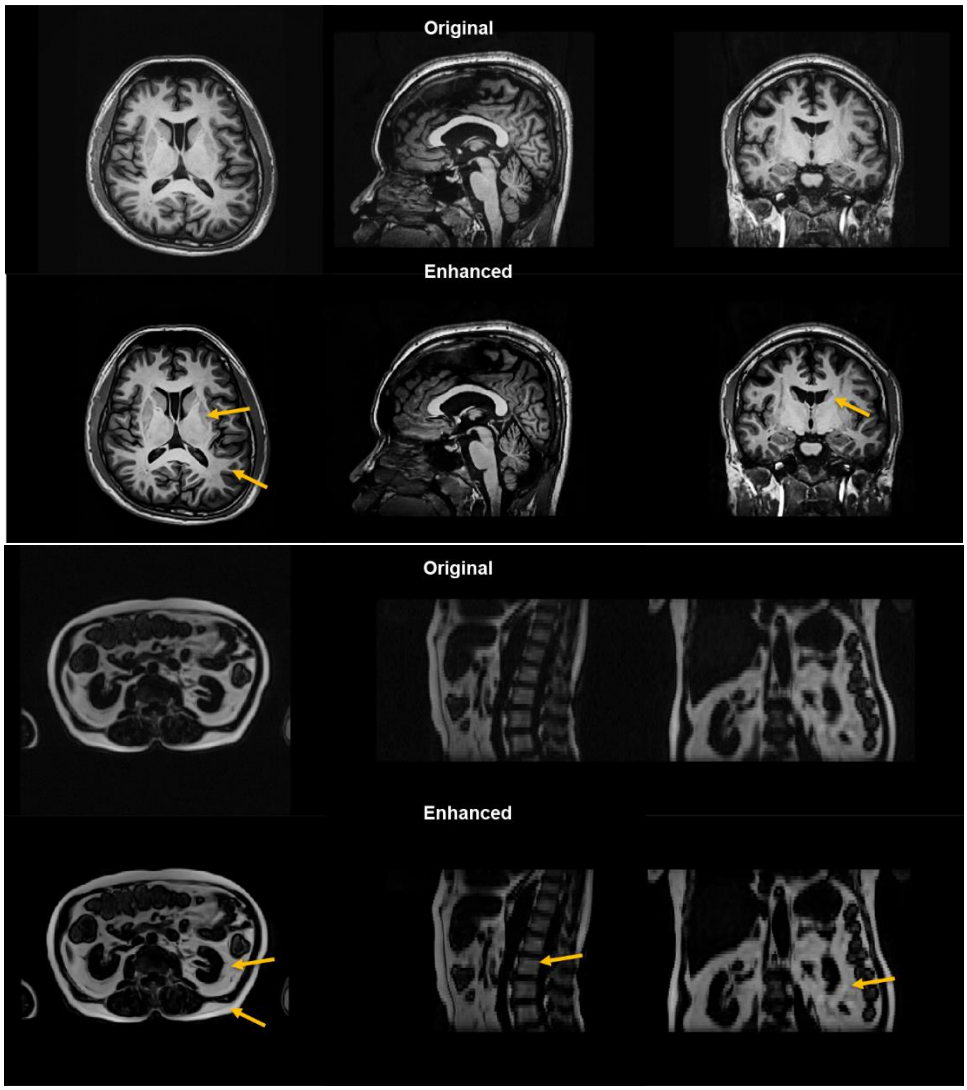


Figure 3a: Comparative analysis of selected samples from a dataset of 500 clinical evaluation scans, showcasing QuickScan enhanced images and standard MRI scans for (A) T_2-weighted imaging of the axial brain Scan. (B) T_2-weighted Axial Abdomen scan (C) T_1-weighted Sagittal lumbar Spine (D) STIR TSE Axial right thigh. QuickScan acquisitions were processed using a post processing algorithm to achieve image quality and anatomical delineation comparable to standard-of-care images. Subjective analysis and clinical validation were performed by investigators, who rated the QuickScan images on a Likert scale of 1 to 10. The ratings indicated 'good' to 'very good' quality, reflecting high organ delineation and overall image quality

Impact of QuickScan Application on Image enhancement – Quantitative and visual evaluation

In brain scans, the average Signal-to-Noise Ratio (SNR) increased significantly from **28.44** to **42.92** ($p<0.001$), while the Contrast-to-Noise Ratio (CNR) rose from **11.88** to **18.03** ($p<0.001$). Abdominal scans demonstrated similar improvements, with the SNR climbing from **35.30** to **50.24** ($p<0.001$) and the CNR increasing significantly from **10,290.93** to **93,767.22** ($p<0.001$). Thigh scans also showed marked improvements, with the SNR increasing from **4.50** to **6.75** ($p<0.001$) and the CNR rising from **5.50** to **7.80** ($p<0.001$). These enhancements underscore QuickScan's effectiveness in improving image quality while preserving anatomical details.



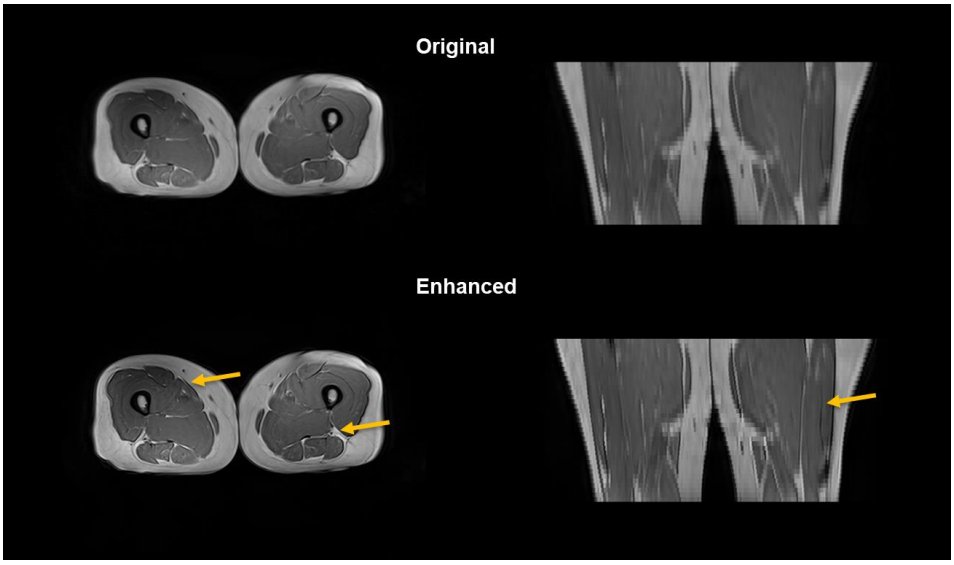


Figure 4 a,b,c: Comparison between the original and QuickScan-enhanced MR images reveals a clear enhancement in image quality, with visibly improved contrast and reduced blur and noise. These improvements are quantitatively supported by increased SNR (Signal-to-Noise Ratio) and CNR (Contrast-to-Noise Ratio) metrics.

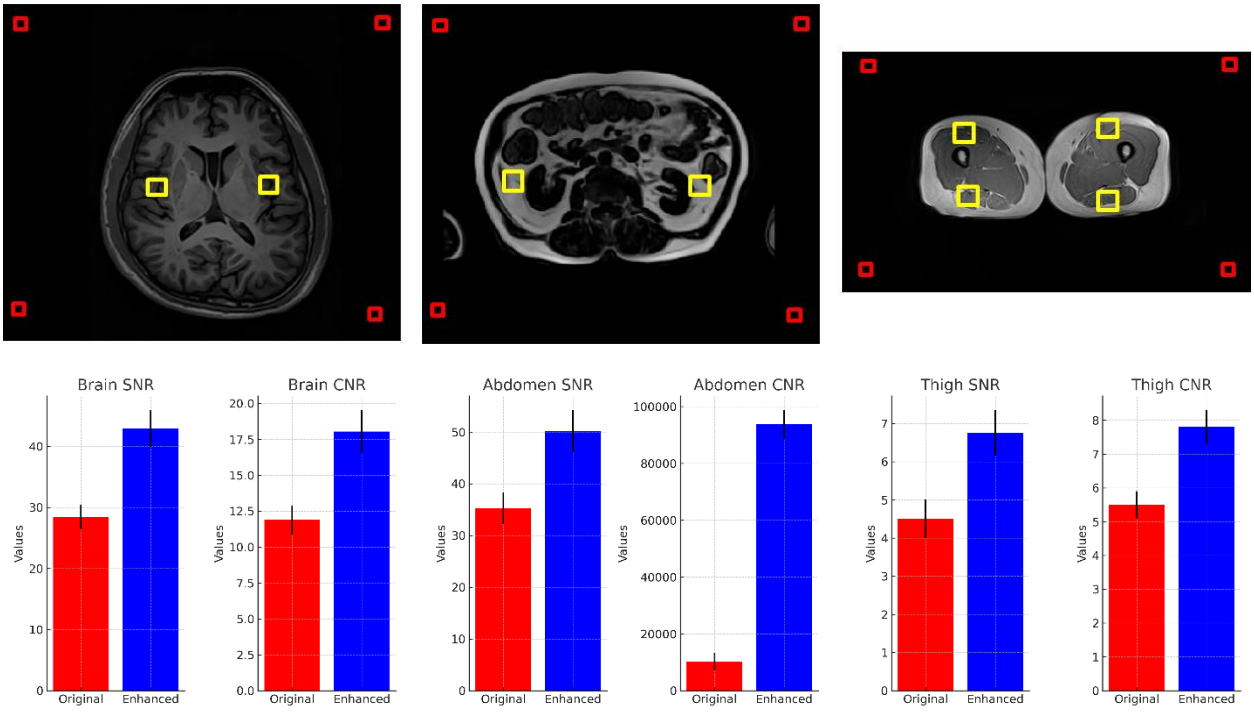


Figure 5 a. Comparative analysis of brain, abdomen, and thigh MRI images before and after QuickScan processing. The figure shows regions of interest (ROIs) for SNR and CNR calculation,

with red squares marking background regions and yellow squares marking signal regions. (b) The bar graph illustrates significant increases in SNR and CNR post-processing, highlighting QuickScan's effectiveness in reducing noise and enhancing contrast to improve clinical evaluation.

Radiologist Evaluation of QuickScan-Enhanced MRI Scans

A double-blinded evaluation conducted by two radiologists (Table 4) highlighted significant improvements in the visibility of intricate anatomical structures and finer intra-structural details in QuickScan-enhanced images. Key enhancements included improved delineation of Intramuscular Adipose Tissue (IMAT), muscle boundaries, tissue-tissue interfaces, and brain structures, along with enhanced bias field correction. These improvements were particularly evident in distinguishing smaller regions that were previously obscured by noise and low contrast. This evaluation reinforces the clinical significance of QuickScan-enhanced images in providing superior diagnostic quality.

Table 4: Double-blinded evaluation scores comparing original and QuickScan-enhanced MR scans for diagnostic quality.

Region	Number of Scans	Scan Type	Radiologist 1 Score	Radiologist 2 Score	Average Score	Improvement
Brain	30	Original	4	6	5	+21
		Enhanced	26	24	25	
Abdomen	40	Original	2	3	2.5	+34.5
		Enhanced	38	37	37.5	
Thigh	35	Original	1	1	1	+33
		Enhanced	34	34	34	

Evaluation of improvement in Segmentation and Quantification with QuickScan-Enhanced Images

Figure 6 displays Dice Similarity Index (DSI) scores comparing original and QuickScan-enhanced MRI scans across different anatomical regions (Supplement Table 1) . QuickScan-enhanced scans exhibited notable improvements in segmentation accuracy:

- **Abdomen:** SSAT improved from 0.97 to 0.98, DSAT from 0.93 to 0.95, and VAT from 0.88 to 0.985.
- **Thigh:** Bone improved from 0.97 to 0.98, IMAT from 0.79 to 0.86, SAT from 0.91 to 0.97, and muscle from 0.72 to 0.87.

- **Brain:** Noise images maintained a DSI of 0.97, while ghost images improved slightly from 0.95 to 0.96.

These improvements highlight QuickScan's effectiveness in enhancing image quality and segmentation accuracy, particularly for complex regions such as thigh IMAT and muscle.

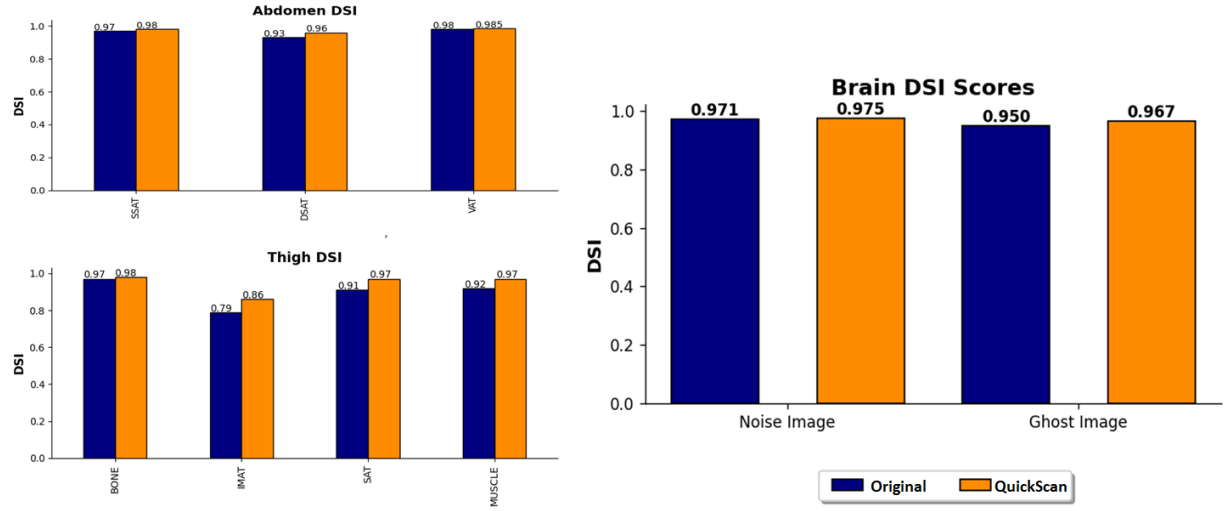


Figure-6. Improvement in Dice Similarity Coefficient (DSC) scores for QuickScan-enhanced images. Bar graphs show increased segmentation accuracy, with AssemblyNet enhancing brain segmentation and Attention Res-UNet improving abdominal and thigh segmentation, demonstrating QuickScan's effectiveness in conjunction with these deep learning models.

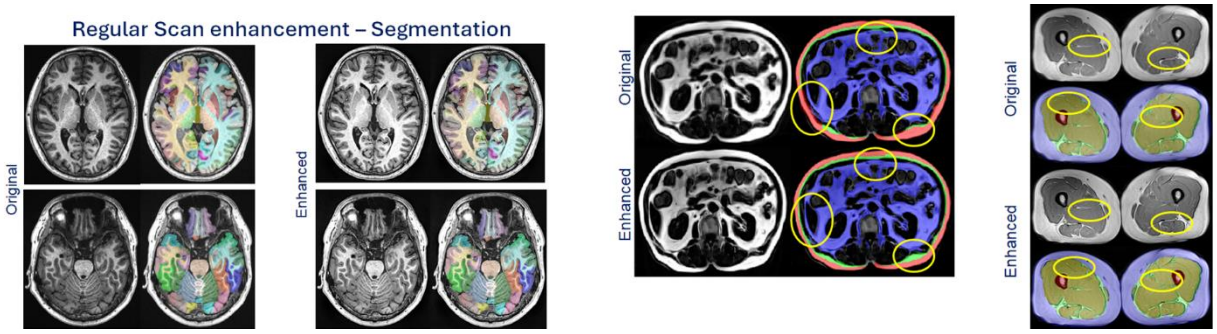


Figure 7: Visual comparison of segmentation results for brain, abdomen, and thigh images before and after QuickScan processing. The figure highlights significant improvements in segmentation accuracy, with QuickScan-enhanced scans showing clearer delineation of anatomical structures. Comparative images emphasize enhanced clarity and precision, particularly in identifying key features. These improvements are supported by increased Dice Similarity Coefficient (DSC) scores, demonstrating QuickScan's effectiveness in improving segmentation accuracy for clinical imaging (see Figure 6).

Discussion

This study evaluated the efficacy of QuickScan application developed by AiKenist, a deep-learning-based post-processing enhancement tool, in improving MRI image quality and reducing scan times. The findings highlight QuickScan's application significant benefits in both time efficiency and image enhancement, contributing to a more efficient, patient-centric MRI workflow. This discussion integrates the results from both phases of the study, addressing the reductions in scan times, improvements in image quality, enhanced segmentation accuracy, and the tool's potential for clinical applications.

Phase 1: Evaluation of QuickScan for Time Efficiency and Visual Quality

Reduced Scan Times with QuickScan application

Our results from Phase 1 suggest that QuickScan significantly streamlines the MRI workflow by reducing scan times across a variety of sequences and anatomical regions (Table -3, Figure -3). This improvement not only alleviates pressure on MRI resources but also enhances patient comfort by reducing the time spent in the scanner. The time-saving potential of QuickScan application was especially evident in T_1- and T_2-weighted sequences used for brain, spine, and musculoskeletal imaging. These findings align with previous studies that emphasize the benefits of AI-based techniques in accelerating MRI acquisition without compromising diagnostic quality [5, 8]. The reduction in scan times is particularly advantageous for patients who may experience discomfort in prolonged scans, such as children and individuals with claustrophobia. Furthermore, faster scan times increase scanner throughput, reduce wait times, and enhance overall departmental efficiency, establishing QuickScan as a valuable tool for optimizing clinical imaging protocols.

Enhanced Image Quality with QuickScan

The enhanced image quality facilitated by QuickScan was quantified through improvements in Signal-to-Noise Ratio (SNR) and Contrast-to-Noise Ratio (CNR) for brain, abdominal, and thigh scans. For example, the SNR for brain scans increased from 28.44 to 42.92 ($p<0.001$) and the CNR from 11.88 to 18.03 ($p<0.001$). For abdominal scans, the SNR rose from 35.30 to 50.24 ($p<0.001$), and CNR improved from 10,290.93 to 93,767.22 ($p<0.001$). These improvements can be attributed to QuickScan's ability to reduce noise and artifacts while preserving crucial anatomical details. Visual comparisons further support these findings (Figure 4). High-quality images are essential for accurate diagnosis, as they enhance the detection of subtle pathological changes. This is

particularly important for early disease detection and timely intervention, where clarity and contrast are paramount.

Phase 2: Segmentation and Quantification with QuickScan-Enhanced Images

Improved Segmentation Accuracy

The enhanced image quality also contributed to improved segmentation accuracy in Phase 2, as reflected in the Dice Similarity Index (DSI) scores. In the abdominal region, DSI scores improved for SSAT (0.97 to 0.98), DSAT (0.93 to 0.95), and VAT (0.88 to 0.985). In the thigh region, DSI scores increased for bone (0.97 to 0.98), IMAT (0.79 to 0.86), SAT (0.91 to 0.97), and muscle (0.72 to 0.87). For brain scans, DSI scores remained high, with noise images at 0.97 and ghost images improving from 0.95 to 0.96. These findings demonstrate that QuickScan-enhanced images enable more accurate segmentation of anatomical regions, which is essential for quantitative analysis and disease monitoring. Improved segmentation accuracy enhances the precision of both diagnostic processes and treatment planning, particularly for monitoring disease progression or surgical planning.

Clinical Applications

Accurate segmentation, especially in muscle and musculoskeletal structures, has important clinical applications. For instance, precise delineation of muscle boundaries is critical for assessing muscle atrophy or hypertrophy, monitoring musculoskeletal disorders, and planning orthopaedic surgeries. These improvements in segmentation accuracy can also be beneficial in a range of clinical settings, such as oncology, neurology, and orthopaedics, where detailed anatomical delineation is vital for accurate diagnosis, treatment planning, and monitoring.

Limitations

While the study results are promising, there are several limitations to consider. The study cohort was relatively small, and further research with larger, more diverse populations is needed to assess the generalizability of the findings. Additionally, the evaluation primarily relied on subjective visual assessments by radiologists. Incorporating objective image quality metrics alongside radiologist evaluations would provide a more comprehensive view of QuickScan’s impact. The study also did not account for variations in scanner hardware and imaging protocols, which could influence the reproducibility and consistency of the results across different clinical settings. Addressing these factors in future studies will be critical to ensuring the robustness and generalizability of QuickScan’s efficacy.

Future Directions

Future research should explore QuickScan’s potential in specific clinical applications, such as evaluating its role in disease diagnosis, treatment planning, and monitoring. Expanding the research scope to include a variety of clinical scenarios will help better understand the practical

utility and limitations of QuickScan-enhanced imaging. Additionally, investigations into the integration of QuickScan with other advanced imaging technologies, such as functional MRI or PET-MRI, could further extend its utility and improve its clinical applications across a broader range of diseases and patient populations.

Conclusion

This study demonstrates significant improvements in MRI image quality and scan time reduction achieved using QuickScan, a deep-learning-based post-processing enhancement tool, for multiple anatomical regions. The SNR increased from 28.44 to 42.92 ($p<0.001$) for brain scans and from 35.30 to 50.24 ($p<0.001$) for abdominal scans. Similarly, the CNR improved from 11.88 to 18.03 ($p<0.001$) for brain scans and from 10,290.93 to 93,767.22 ($p<0.001$) for abdominal scans. These enhancements in image quality led to significant improvements in segmentation accuracy.

The Dice Similarity Index (DSI) increased for key anatomical regions in QuickScan-enhanced images. For the abdomen, DSI values rose from 0.97 to 0.98 for SSAT, from 0.93 to 0.95 for DSAT, and from 0.88 to 0.985 for VAT. Thigh segmentation showed notable improvements, with muscle DSI increasing by 21% (0.72 to 0.87) and IMAT DSI increasing by 9% (0.79 to 0.86). These results confirm that QuickScan enhances segmentation model performance by providing higher-quality inputs for analysis and monitoring of anatomical structures.

QuickScan also reduced MRI scan times by an average of 0.91 to 1.76 minutes, particularly for T_1- and T_2 – weighted sequences. This improvement increases scanner throughput and enhances patient comfort, especially in pediatric and emergency imaging scenarios, where fast and high-quality imaging is essential.

References

1. Haacke, E. M., & Tkach, J. A. (1990). Fast MR imaging: techniques and clinical applications. *AJR American Journal of Roentgenology, 155*(5), 951-964. https://doi.org/10.2214/ajr.155.5.2120964
2. Pfeifer, C. M. (2018). Rapid-sequence MRI of the brain: A distinct imaging study. *AJNR American Journal of Neuroradiology, 39*(8), E93-E94. https://doi.org/10.3174/ajnr.A5685
3. Karantanas, A. H., Zibis, A. H., & Papanikolaou, N. (2000). Comparison of echo planar imaging, gradient echo, and fast spin echo MR scans of knee menisci. *Computerized Medical Imaging and Graphics, 24*(5), 309-316. https://doi.org/10.1016/s0895-6111(00)00027-6
4. Zaitsev, M., Maclaren, J., & Herbst, M. (2015). Motion artifacts in MRI: A complex problem with many partial solutions. *Journal of Magnetic Resonance Imaging, 42*(4), 887-901. https://doi.org/10.1002/jmri.24850
5. Beall, D. P., Fortman, B. J., Lawler, B. C., & Regan, F. (2002). Imaging bowel obstruction: A comparison between fast magnetic resonance imaging and helical computed tomography. *Clinical Radiology, 57*(8), 719-724. https://doi.org/10.1053/crad.2001.0735
6. Chen, Z., Pawar, K., Ekanayake, M., Pain, C., Zhong, S., & Egan, G. F. (2023). Deep learning for image enhancement and correction in magnetic resonance imaging-state-of-the-art and challenges. *Journal of Digital Imaging, 36*(1), 204-230. https://doi.org/10.1007/s10278-022-00721-9
7. Zhu, G., Jiang, B., Tong, L., Xie, Y., Zaharchuk, G., & Wintermark, M. (2019). Applications of deep learning to neuro-imaging techniques. *Frontiers in Neurology, 10*, 869. https://doi.org/10.3389/fneur.2019.00869
8. Rudie, J. D., Gleason, T., Barkovich, M. J., Wilson, D. M., Shankaranarayanan, A., Zhang, T., Wang, L., Gong, E., Zaharchuk, G., &

Villanueva-Meyer, J. E. (2022). Clinical assessment of deep learning-based super-resolution for 3D volumetric brain MRI. *Radiology: Artificial Intelligence*, *4*(2), e210059. .

9. Almansour, H., Herrmann, J., Gassenmaier, S., Lingg, A., Nickel, M., Kannengiesser, S., Arberet, S., Othman, A., & Afat, S. (2022). Combined deep learning-based super-resolution and partial Fourier reconstruction for gradient echo sequences in abdominal MRI at 3 Tesla: Shortening breath-hold time and improving image sharpness and lesion conspicuity. *Academic Radiology*. https://doi.org/10.1016/j.acra.2022.06.003
10. Chu, B., Gan, L., Shen, Y., Song, J., Liu, L., Li, J., & Liu, B. (2023). A deep learning image reconstruction algorithm for improving image quality and hepatic lesion detectability in abdominal dual-energy computed tomography: Preliminary results. *Journal of Digital Imaging*, *36*, 763–771. https://doi.org/10.1007/s10278-023-00893-y
11. Zhang, Z., Yang, Y., Yuan, Y., & Chen, Q. (2021). Enhancing the reconstruction process of undersampled non-Cartesian dynamic abdominal MRI data using deep learning-based convolutional recurrent neural networks. *Medical Image Analysis*, *68*, 101857. https://doi.org/10.1016/j.media.2020.101857
12. Kim, H. K., Kim, Y., Lee, S., Kang, H., & Park, S. (2023). Deep learning-based k-space-to-image reconstruction and super-resolution for diffusion-weighted imaging in whole-spine MRI. *Magnetic Resonance in Medicine*, *89*(1), 215–229. https://doi.org/10.1002/mrm.28542
13. Racine, D., Becce, F., Rizzo, E., Verdun, F. R., & Bochud, F. O. (2020). Performance of deep learning-based image reconstruction for low-dose abdominal CT in a prospective clinical study. *Radiology*, *297*(2), 442–451. https://doi.org/10.1148/radiol.2020200746
14. Bornet, P. A., Villani, N., Gillet, R., Germain, E., Lombard, C., Blum, A., & Teixeira, P. G. (2022). Clinical acceptance of deep learning reconstruction for abdominal CT imaging: Objective and subjective image quality and low-contrast detectability assessment. *European Radiology*, *32*(5), 3151–3162. https://doi.org/10.1007/s00330-021-08410-x
15. Wang, X., Yu, K., Dong, C., & Change Loy, C. (2018). ESRGAN: Enhanced Super-Resolution Generative Adversarial Networks. *Proceedings of the European Conference on Computer Vision Workshops (ECCVW)*, 63–79. https://doi.org/10.1007/978-3-030-11021-5_5
16. Zhang, Y., Tian, Y., Kong, Y., Zhong, B., & Fu, Y. (2018). Residual Dense Network for Image Super-Resolution. *IEEE Conference on Computer Vision and Pattern Recognition (CVPR)*, 2472–2481. https://doi.org/10.1109/CVPR.2018.00262
17. Huang, G., Liu, Z., van der Maaten, L., & Weinberger, K. Q. (2017). Densely connected convolutional networks. *IEEE Conference on Computer Vision and Pattern Recognition (CVPR)*, 4700–4708. https://doi.org/10.1109/CVPR.2017.243
18. Lim, B., Son, S., Kim, H., Nah, S., & Mu Lee, K. (2017). Enhanced Deep Residual Networks for Single Image Super-Resolution. *Proceedings of the IEEE Conference on Computer Vision and Pattern Recognition Workshops (CVPRW)*, 1132–1140. https://doi.org/10.1109/CVPRW.2017.151
19. Vaswani, A., Shazeer, N., Parmar, N., Uszkoreit, J., Jones, L., Gomez, A. N., Kaiser, Ł., & Polosukhin, I. (2017). Attention is all you need. *Advances in Neural Information Processing Systems (NeurIPS)*, 5998–6008. https://arxiv.org/abs/1706.03762

20. Ledig, C., Theis, L., Huszár, F., Caballero, J., Aitken, A. P., Tejani, A., Totz, J., Wang, Z., & Shi, W. (2017). Photo-realistic single image super-resolution using a generative adversarial network. *IEEE Conference on Computer Vision and Pattern Recognition (CVPR)*, 4681–4690. https://doi.org/10.1109/CVPR.2017.19
21. Johnson, J., Alahi, A., & Fei-Fei, L. (2016). Perceptual losses for real-time style transfer and super-resolution. *Proceedings of the European Conference on Computer Vision (ECCV)*, 694–711. https://doi.org/10.1007/978-3-319-46475-6_43
22. Coupé, P., Mansencal, B., Clément, M., Giraud, R., Senneville, B.D., Thong, T.V., Lepetit, V., & Manjón, J.V. (2019). AssemblyNet: A large ensemble of CNNs for 3D whole brain MRI segmentation. *NeuroImage, 219*.
23. Denis de Senneville, B., Manjón, J.V., & Coupé, P. (2020). RegQCNET: Deep quality control for image-to-template brain MRI affine registration. *Physics in Medicine & Biology, 65*.
24. AssemblyNet. (n.d.). AssemblyNet: A robust framework for brain MRI segmentation. GitHub repository. Retrieved from https://github.com/volBrain/AssemblyNet
25. Luong, M-T., Pham, H. & Manning, C. D. Effective approaches to attention-based neural machine translation. arXiv Prepr. arXiv:1508.04025 (2015).
26. Wang, X., Girshick, R., Gupta, A. & He, K. Non-local neural networks. In Proceedings of the IEEE Conference on Computer Vision and Pattern Recognition 7794–7803 (2018).
27. Anderson, P., He, X., Buehler, C., Teney, D., Johnson, M., Gould, S. & Zhang, L. Bottom-up and top-down attention for image captioning and visual question answering. In Proceedings of the IEEE Conference on Computer Vision and Pattern Recognition 6077–6086 (2018).
28. Jetley, S., Lord, N. A., Lee, N. & Torr, P. H. Learn to pay attention. In International Conference on Learning Representations https://openreview.net/forum?id=HyzbhfWRW (2018
29. Wang, Z., Bovik, A. C., Sheikh, H. R., & Simoncelli, E. P. (2004). Image quality assessment: From error visibility to structural similarity. *IEEE Transactions on Image Processing*, *13*(4), 600–612. https://doi.org/10.1109/TIP.2003.819861
30. Dietrich, O., Raya, J. G., Reeder, S. B., Reiser, M. F., & Schoenberg, S. O. (2007). Measurement of signal-to-noise ratios in MR images: Influence of multi-channel coils, parallel imaging, and reconstruction filters. *Journal of Magnetic Resonance Imaging*, *26*(2), 375–385. https://doi.org/10.1002/jmri.20969

Supplementary Table 1

Table S1: Reports the Dice Similarity Index (DSI) scores for abdomen, thigh, and brain scans, comparing the performance of the Original and QuickScan methods. Improvements in DSI scores across various regions, including adipose tissue, muscle, and bone, are highlighted. Table 5a: Abdomen DSI Scores, Table 5b: Thigh DSI Scores, Table 5c: Brain DSI Scores

Region	**Metric**	**Original (DSI ± STD)**	**QuickScan (DSI ± STD)**	**Original (HD ± STD, mm)**	**QuickScan (HD ± STD, mm)**
SSAT	**Training**	0.963 ± 0.012	0.973 ± 0.010	3.21 ± 0.45	2.80 ± 0.40
	Testing	0.970 ± 0.013	0.980 ± 0.011	3.50 ± 0.50	2.95 ± 0.42
DSAT	**Training**	0.925 ± 0.015	0.950 ± 0.012	4.10 ± 0.55	3.70 ± 0.45
	Testing	0.930 ± 0.016	0.960 ± 0.012	4.30 ± 0.60	3.90 ± 0.50
VAT	**Training**	0.975 ± 0.011	0.985 ± 0.010	2.90 ± 0.40	2.50 ± 0.35
	Testing	0.980 ± 0.012	0.987 ± 0.011	3.10 ± 0.45	2.70 ± 0.38

Dataset	**Metric**	**Bone**	**IMAT**	**Muscle**	**SAT**
Training (Original)	**DSI**	0.9827 ± 0.004	0.9360 ± 0.010	0.9739 ± 0.020	0.9793 ± 0.007
	HD (mm)	2.064 ± 0.440	3.747 ± 0.503	3.039 ± 0.624	3.713 ± 0.505
	DSI	0.9891 ± 0.001	0.9760 ± 0.240	0.9899 ± 0.003	0.9894 ± 0.038

Training (QuickScan)	**HD (mm)**	1.888 ± 0.520	2.147 ± 0.201	2.039 ± 0.111	2.714 ± 0.201
Testing (Original)	**DSI**	0.9771 ± 0.025	0.7916 ± 0.012	0.9106 ± 0.005	0.9227 ± 0.013
	HD (mm)	2.342 ± 0.500	4.941 ± 0.407	3.980 ± 0.578	3.147 ± 0.454
Testing (QuickScan)	**DSI**	0.9872 ± 0.032	0.8647 ± 0.023	0.9752 ± 0.010	0.9727 ± 0.013
	HD (mm)	2.374 ± 0.598	5.350 ± 0.482	4.474 ± 0.778	5.332 ± 0.479

Dataset	**Metrics (Testing)**	**Label 1.0**	**Label 2.0**	**Label 3.0**	**Label 4.0**	**Label 5.0**	**Label 6.0**	**Label 7.0**	**Overall DSI Score**
Original Dataset	**Brain MR Noise Scan**	0.927 ± 0.038	0.974 ± 0.013	0.978 ± 0.011	0.981 ± 0.009	0.984 ± 0.008	0.972 ± 0.014	0.981 ± 0.012	**0.971**
	Brain MR Ghost Scan	0.877 ± 0.028	0.956 ± 0.010	0.961 ± 0.010	0.971 ± 0.013	0.969 ± 0.011	0.936 ± 0.029	0.981 ± 0.016	**0.950**
QuickScan Dataset	**Brain MR Noise Scan**	0.884 ± 0.025	0.960 ± 0.008	0.965 ± 0.007	0.971 ± 0.006	0.977 ± 0.005	0.958 ± 0.010	0.977 ± 0.008	**0.975**
	Brain MR Ghost Scan	0.864 ± 0.283	0.950 ± 0.314	0.956 ± 0.316	0.966 ± 0.319	0.966 ± 0.321	0.931 ± 0.312	0.974 ± 0.320	**0.967**